

Temporal and Volumetric Denoising via Quantile Sparse Image (QuaSI) Prior in Optical Coherence Tomography and Beyond

Franziska Schirrmacher^{1,*}, Thomas Köhler^{1,4,*}, Tobias Lindenberger¹,
 Lennart Husvogt¹, Jürgen Endres^{1,3}, James G. Fujimoto², Joachim Hornegger¹,
 Arnd Dörfler³, Philip Hoelter³, and Andreas K. Maier¹

¹ Pattern Recognition Lab, Friedrich-Alexander-Universität Erlangen-Nürnberg,
 Germany

{franziska.schirrmacher, thomas.koehler}@fau.de

² Department of Electrical Engineering & Computer Science and Research Laboratory
 of Electronics, Massachusetts Institute of Technology, USA ³Department of
 Neuroradiology, Universitätsklinikum Erlangen, Germany ⁴e.solutions GmbH,
 Erlangen, Germany

* These authors contributed equally to this work.

Abstract. This paper introduces an universal and structure-preserving regularization term, called quantile sparse image (QuaSI) prior. The prior is suitable for denoising images from various medical image modalities. We demonstrate its effectiveness on volumetric optical coherence tomography (OCT) and computed tomography (CT) data, which show different noise and image characteristics. OCT offers high-resolution scans of the human retina but is inherently impaired by speckle noise. CT on the other hand has a lower resolution and shows high-frequency noise. For purpose of denoising, we propose a variational framework based on the QuaSI prior and a Huber data fidelity model that can handle 3-D and 3-D+t data. Efficient optimization is facilitated through use of an alternating direction method of multipliers (ADMM) scheme and the linearization of the quantile filter. Experiments on multiple dataset emphasize the excellent performance of the proposed method.

1 Introduction

Optical coherence tomography (OCT) is a standard non-invasive imaging modality within clinical workflows in ophthalmology. A fine spatial resolution and the possibility of 3-D imaging aid the diagnosis and monitoring of eye diseases. In OCT, low-coherent light passes through an interferometer-like setting and is reflected back by the object. The amount of back-reflections in a certain axial depth determines the amplitude of an interference signal at one position. From the interference signal one can obtain depth-layers of the object. There are two different types of systems: time domain OCT (TD-OCT) and Fourier domain OCT (FD-OCT). In TD-OCT, light is decomposed into two parts and propagated

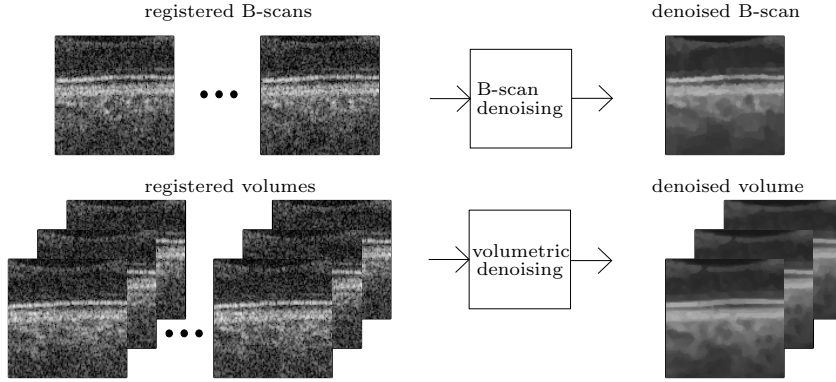


Fig. 1: We propose two pipelines of our spatio-temporal denoising algorithm for OCT data. In the first pipeline (top), hereinafter called *B-scan denoising*, single B-scans or a sequence of registered B-scans are processed. The second pipeline (bottom) processes volumes as well as a sequence of registered volumes and is called *volumetric denoising*.

through a sample and a reference arm. The light is reflected back by a mirror to assign the reflected light in the sample arm to an axial depth. In FD-OCT, the Fourier transform enables a spectral resolution of the interference signal, without scanning the reference arm. Predefined patterns are used to scan an object. At each position a 1-D *A-Scan* is obtained encoding the back scatter intensities in axial depth. A 2-D *B-Scan* comprises multiple of these A-Scans acquired with linear or circular scan patterns. Current OCT systems also provide volumetric data called *C-scans*. To this end, several parallel B-scans are conducted with high speed to obtain 3-D volumes.

Photon interference during the acquisition causes *speckle noise*, which turns out to be a major drawback of OCT. As a consequence, the quality of the scans might be drastically reduced. This can limit the reliability of OCT in diagnostic workflows [12] or affects image analysis for computer-aided diagnostics. Denoising of OCT to mitigate these limitations emerged as an active research area within the field of retinal image processing. In general, it can be approached using customized hardware [21,7], spatial filtering of single scans [19,8], or temporal merging of multiple consecutive scans [17]. However, denoising is still a challenging task due to two reasons: 1) OCT measures fine morphological structures and it would be unacceptable regarding clinical applications to impair these structures. 2) The inferring speckle noise follows a multiplicative model, which violates the assumption on the noise statistics of most popular denoising methods that emerged in the image processing community.

In this paper, we propose denoising by *postprocessing* noisy OCT scans within a variational framework. As the key contribution, we introduce the class of *quantile sparse image* (QuaSI) priors to model the appearance of noise-free OCT data. Specifically, we propose a median filter based regularizer that is based

on the QuaSI prior using the 0.5 quantile. This follows the idea that a noise-free scan should be a fixed point of the median filter and we show that this approach facilitates structure-preserving denoising. To approach the resulting non-linear and non-convex optimization derived in our framework, we present an alternating direction method of multipliers (ADMM) scheme. Our algorithm can handle *spatio-temporal* denoising by processing either single scans or sequences of consecutive scans. Furthermore, it enables denoising on a B-scan level or on a volume level. Thus, it can be adjusted to the clinical needs within a target application. The proposed method can also be integrated to commercial OCT systems without modifications on the existing hardware or scanning protocols.

This paper is an extension of our prior work in [25] and makes the following additional contributions:

- The algorithm as well as the QuaSI prior are extended to process volumetric OCT data.
- An investigation of the convergence and parameter sensitivity of the algorithm is conducted.
- An extension of our algorithm is presented to process volumetric data in C-arm CT imaging.

The remainder of this paper is organized as follows. In Section 2, we review related work on OCT denoising. Section 3 comprises the objective function of the energy minimization problem. In Section 4 the QuaSI prior is introduced. The numerical optimization of our denoising framework is derived in Section 5. In Section 6, an experimental evaluation of our method on publicly available benchmark data and clinical OCT scans as well as CT data is reported. Finally, Section 7 contains our conclusion.

2 Related work

The image-based techniques can be divided into two groups.

2.1 Spatial Denoising Methods

Spatial or *single-image* denoising have been extensively studied in the image processing community and various approaches emerged over the past decades. Local image filters performs smoothing of noisy images possibly in an adaptive way to preserve image structures [27]. Non-local filtering also exploits the statistics of similar and repeating patches within images. One representative from this class is the successful BM3D method [5]. However, these methods have been mainly designed for natural images under simplified assumptions like additive white Gaussian noise, which is inappropriate to describe speckle noise that is multiplicative in nature. Learning-based denoising, e.g. based on multilayer neural networks [3], hold the potential to handle speckle noise by learning noise distributions from training data. However, large-scale training data required for such methods is barely available for OCT.

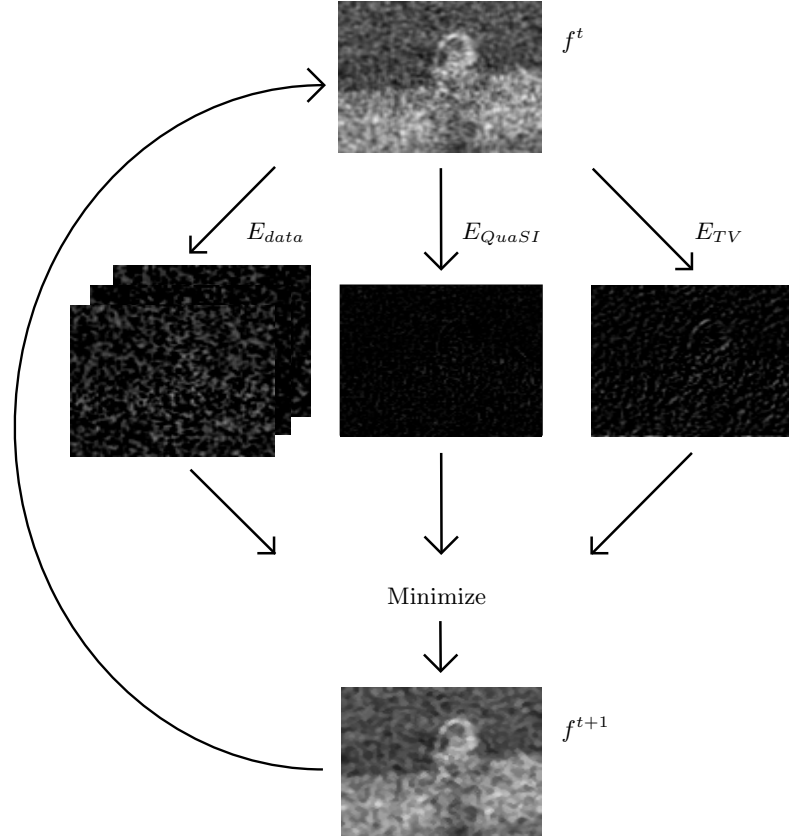


Fig. 2: Method overview: The proposed spatio-temporal denoising algorithm is based on an energy minimization formulation with three terms.

Some spatial filters that have been adopted for OCT denoising are the hybrid median filter, Lee filter, Wiener filter, or wavelet thresholding as investigated by Ozcan *et al.* [19]. Global denoising methods for OCT have been introduced by Salinas *et al.* [24] using non-linear diffusion and later by Duan *et al.* [8] using second order total generalized variation. Wong *et al.* [30] have proposed structure-adaptive Bayesian estimation to handle speckle noise. One interesting approach has been proposed Fang *et al.* [9], where dictionary learning based on B-scans with high signal-to-noise ratio (SNR) is used to denoise low SNR B-scans.

Single-image denoising offers great flexibility in clinical applications of OCT as few assumption on the the scanning protocol are made. However, the noise reduction is limited as such methods can utilize single B-scans only.

2.2 Temporal Denoising Methods

Temporal or *multi-image* denoising methods considers coherence of consecutive images to improve noise reduction over single-image denoising. Such methods have been widely investigated for OCT and exploit sets of B-scans that are acquired sequentially from the same location or nearby positions. A popular approach in commercial systems is to register multiple of these B-scans and to average the registered scans to cancel out random noise. Averaging is computationally efficient but requires many repetitive acquisitions to effectively reduce speckle noise. Mayer *et al.* [17] enhances simple averaging based on wavelet decompositions of B-scans to estimate local image structures and noise. Denoising is conducted in the wavelet domain by weighted averaging of wavelet coefficients according to the local image structure. Cheng *et al.* [4] formulates OCT denoising from multiple scans as a low-rank matrix completion problem. In [26], Thapa *et al.* follows a similar notion and exploits the low-rank property on patch-based level of multiple B-scans using weighted nuclear norm minimization. Bian *et al.* [2] have proposed inter-frame and intra-frame priors for denoising using convex optimization.

All of these multi-image methods have in common that they require multiple input scans. This increases the overall acquisition time and therefore they might lead to a higher patient discomfort. Also, they perform denoising on a B-scan level but ignore coherence of nearby B-scans within volumetric OCT data. If denoising of entire volumes is desired, simple consecutive processing of individual B-scans can lead to suboptimal results. In this paper, we mitigate both limitations by proposing a unified approach to handle denoising on B-scan or volume level based on single or multiple scans.

3 Background

This section presents the variational framework for denoising volumetric OCT data. Fig. 1 illustrates the two pipelines of our proposed algorithm, namely B-scan denoising and volumetric denoising. We denote a volume as a tensor $\tilde{\mathbf{G}} \in \mathbb{R}^{L \times N_x \times N_y}$ composed of L B-scans $\tilde{\mathbf{G}}_l$, $l = 1, \dots, L$ of size $N_x \times N_y$ pixels. For the sake of convenience, we reshape volumes to vector notation according to $\tilde{\mathbf{g}} = (\tilde{\mathbf{g}}_1, \dots, \tilde{\mathbf{g}}_L)^\top \in \mathbb{R}^{LN}$, where $\tilde{\mathbf{g}}_l \in \mathbb{R}^N$, $N = N_x N_y$ denotes a single B-scan using row-wise scanning of $\tilde{\mathbf{G}}_l$.

3.1 Noise Model

In OCT, each captured B-scan $\tilde{\mathbf{g}}_l$ of a volume $\tilde{\mathbf{g}}$ is related to a respective noise-free scan $\tilde{\mathbf{f}}_l$ in a volume $\tilde{\mathbf{f}} = (\tilde{\mathbf{f}}_1, \dots, \tilde{\mathbf{f}}_L)^\top \in \mathbb{R}^{LN}$ according to the multiplicative model:

$$\tilde{\mathbf{g}}_l = \tilde{\mathbf{f}}_l \odot \tilde{\mathbf{n}}_l, \quad (1)$$

where \odot is the Hadamard (element-wise) product and $\tilde{\mathbf{n}}_l \in \mathbb{R}^N$ denotes multiplicative speckle noise. Following prior work on OCT denoising [30,8], we formulate the multiplicative noise model in (1) in a logarithmic measurement domain. This leads to the additive noise model:

$$\mathbf{g}_l = \mathbf{f}_l + \mathbf{n}_l, \quad (2)$$

where $\mathbf{g}_l = \log(\tilde{\mathbf{g}}_l)$, $\mathbf{f}_l = \log(\tilde{\mathbf{f}}_l)$ and $\mathbf{n}_l = \log(\tilde{\mathbf{n}}_l)$.

3.2 Energy Minimization Formulation

Given a sequence of $K \geq 1$ volumes $\mathbf{g}^{(k)}$ with $k = 1, \dots, K$ that are either captured from the same position or from nearby positions and registered to each other, we aim at finding a noise-free volume $\hat{\mathbf{f}}$. We formulate denoising as the minimization of the objective function:

$$\hat{\mathbf{f}} = \underset{\mathbf{f}}{\operatorname{argmin}} \sum_{k=1}^K \rho(\mathbf{f} - \mathbf{g}^{(k)}) + \lambda R_{\text{QuaSI}}(\mathbf{f}) + \mu \|\nabla \mathbf{f}\|_1. \quad (3)$$

The first term in (3) denotes the data fidelity of \mathbf{f} w.r.t. input volumes $\mathbf{g}_1, \dots, \mathbf{g}_L$ followed by two regularization terms. The first regularization term is the proposed quantile sparse image (QuaSI) prior weighted by $\lambda \geq 0$. The second regularization term denotes $\mu \geq 0$ weighted anisotropic total variation (TV), which regularizes the image gradient $\nabla \mathbf{f} = (\nabla_x \mathbf{f}, \nabla_y \mathbf{f}, \nabla_z \mathbf{f})^\top$. It is worth noting that the general denoising framework in (3) can handle both noise reduction for entire volumes in 3-D as well as for individual B-scans in 2-D by constraining the domain of both regularization terms.

In (3), the data fidelity term is customized to the image formation in OCT using the loss function $\rho : \mathbb{R}^N \rightarrow \mathbb{R}_0^+$. In general, the image formation for clinical OCT needs to consider a mixture of speckle noise, potential misalignments between the input volumes, or motion artifacts. Following prior work on mixed noise models in image restoration [11], we propose to use the Huber loss [18]:

$$\rho(\mathbf{z}) = \sum_{i=1}^N \phi(z_i), \quad (4)$$

where:

$$\phi(z) = \begin{cases} \frac{1}{2}z^2 & \text{if } z \leq \epsilon \\ \epsilon(|z| - \frac{1}{2}\epsilon) & \text{otherwise,} \end{cases} \quad (5)$$

and $\epsilon > 0$ denotes the threshold of the Huber loss. This leads to an outlier-insensitive model while the underlying data fidelity is a convex term.

4 Quantile Sparse Image (QuaSI) Prior

A robust and efficient regularization term is of importance to achieve results with a high signal-to-noise ratio (SNR). The better the regularization term is able to

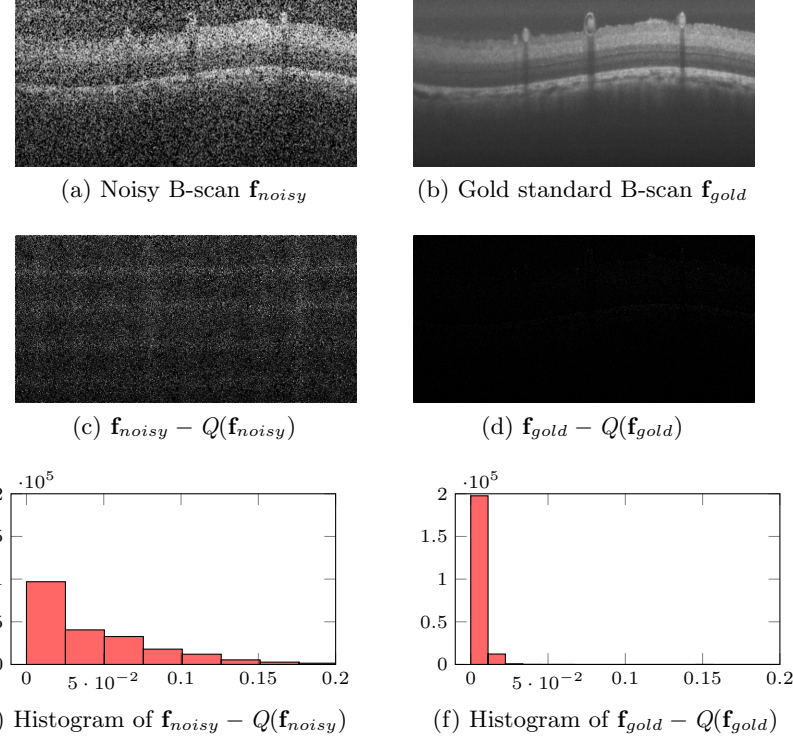


Fig. 3: Analysis of our proposed QuaSI prior using median filtering $Q(\cdot)$ to model the appearance of OCT B-scans. (a) and (b) depict a noisy B-scan along the respective gold standard taken from the pig eye dataset [17]. (c) and (d) show the residual $\mathbf{f} - Q(\mathbf{f})$ of the QuaSI regularization term, where brighter pixels express higher residuals (contrast enhanced for visualization). (e) and (f) depict the corresponding histograms of the both residuals, where the histogram for the gold standard is sparse. Our QuaSI prior exploits the sparsity of $\mathbf{f} - Q(\mathbf{f})$ for regularization in our variational denoising framework.

model natural or medical images, the better the result of the optimization. In OCT denoising structure preservation is a sensitive issue. The B-scans contain small morphological structures that need to be preserved for the purpose of diagnosis. In order to tackle the problems referred to above, the so called quantile sparse image (QuaSI) prior is introduced.

4.1 Definition of the Prior

The QuaSI prior is based on quantile filtering, where the quantile filter is denoted as $\hat{\mathbf{f}} = Q(\mathbf{f})$. The p -quantile with $p \in [0, 1]$ is determined within a local neighborhood $\mathcal{N}(i)$, where d denotes the width of the cubic filter kernel. For

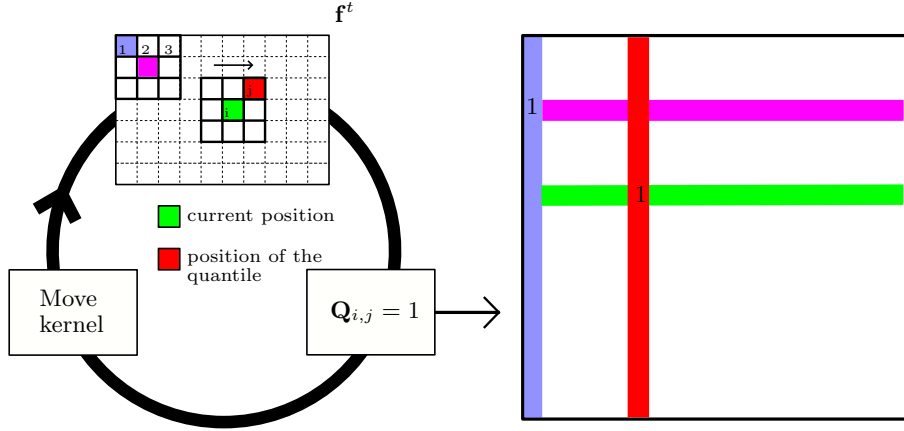


Fig. 4: Construction of the binary matrix to approximate the quantile filter $Q(\mathbf{f}) = \mathbf{Q}\mathbf{f}^t$.

the i -th pixel in \mathbf{f} we filter according to $\tilde{f}_i = \text{quantile}_{\mathcal{N}(i)}(f_i, p)$. Inspired by the regularization by denoising priors by [22], the denoised volume is a fixed point under the quantile filter. In this way:

$$R_{\text{QuaSI}}(\mathbf{f}) = \|\mathbf{f} - Q(\mathbf{f})\|_1. \quad (6)$$

Specifically, regularization according to (6) enforces sparsity of residual $\mathbf{f} - Q(\mathbf{f})$. This offers a general model for regularization and – depending on the application – various types of statistics can be chosen for $Q(\mathbf{f})$. In this paper, we propose the median filter, where $\tilde{f}_i = \text{median}_{\mathcal{N}(i)}(f_i)$. This follows the rationale that median filtering facilitates structure-preserving denoising under non-Gaussian noise.

To validate the QuaSI prior using median filter regularization for OCT denoising, we study its behavior under real measurement noise. For this purpose, we use the publicly available pig eye dataset [17], which provides a gold standard B-scan obtained from the average of 455 registered noisy B-scans. We compare a noisy B-scan $\mathbf{f}_{\text{noisy}}$ with the gold standard \mathbf{f}_{gold} in Fig. 3a and Fig. 3b. The residuals $\mathbf{f} - Q(\mathbf{f})$ of the QuaSI regularization term are illustrated in Fig. 3c for the noisy B-scan and in Fig. 3d for the gold standard. Compared to the gold standard, the noisy B-scan yields a less sparse signal as shown in the histograms of both residuals in Fig. 3e and Fig. 3f. Notice that the QuaSI regularization does not penalize image discontinuities. The histogram using the noisy B-scan contains less zero elements, while the histogram for the gold standard is sparse. Our proposed QuaSI prior exploits these observations for structure-preserving regularization in our variational denoising framework.

4.2 Linearization

In order to deal with the non-linearity of the quantile operator $Q(\mathbf{f})$ the linearization $Q(\mathbf{f}) = \mathbf{Q}\mathbf{f}$, similar to the work of [20], is performed. The binary matrix \mathbf{Q} is assembled element-wise according to:

$$Q_{ij} = \begin{cases} 1 & \text{if } j = z, \\ 0 & \text{otherwise,} \end{cases} \quad (7)$$

where $z = \arg \text{quantile}_{r \in \mathcal{N}(i)} f_r$. This operation filters the i -th pixel according to the p -quantile in its local neighborhood $\mathcal{N}(i)$. For $\mathbf{f}' = \mathbf{f}$ the linearization fulfills $Q(\mathbf{f}') = \mathbf{Q}\mathbf{f}'$, while otherwise \mathbf{Q} serves as an approximation of the quantile filter.

Fig. 4 illustrates the construction of the binary matrix \mathbf{Q} in 2-D. Each pixel is replaced by the quantile within its local neighborhood. The position of the quantile is stored in the binary matrix. In this example, the quantile is at position j . Thus, the i row of the matrix contains a one in the j -th column and zeros otherwise. The multiplication $\mathbf{Q}\mathbf{f}$ yields the quantile filtered result.

5 Deploying QuaSI for OCT Denoising

The non-smooth and non-linear QuaSI prior as well as the non-smooth TV prior impede the optimization of (3) due to the quantile filter and the L_1 -Norm. Using the linearization of the quantile filter and an optimization scheme based on ADMM [10] enable an efficient minimization. In order to tackle the L_1 -Norm, the auxiliary variables \mathbf{u} and \mathbf{v} are introduced. This leads to the constraint optimization problem:

$$\begin{aligned} \hat{\mathbf{f}} = \arg \min_{\mathbf{f}} & \sum_{k=1}^K \rho(\mathbf{f} - \mathbf{g}^{(k)}) + \lambda \|\mathbf{u}\|_1 + \mu \|\mathbf{v}\|_1 \\ \text{such that } & \mathbf{u} = \mathbf{f} - Q(\mathbf{f}), \mathbf{v} = \nabla \mathbf{f}. \end{aligned} \quad (8)$$

An unconstrained optimization problem is obtained using quadratic penalty functions according to:

$$\begin{aligned} \hat{\mathbf{f}} = \arg \min_{\mathbf{f}} & \sum_{k=1}^K \rho(\mathbf{f} - \mathbf{g}^{(k)}) + \frac{\alpha}{2} \|\mathbf{u} - \mathbf{f} + Q(\mathbf{f})\|_2^2 + \lambda \|\mathbf{u}\|_1 \\ & + \frac{\beta}{2} \|\mathbf{v} - \nabla \mathbf{f}\|_2^2 + \mu \|\mathbf{v}\|_1. \end{aligned} \quad (9)$$

The Lagrangian multipliers $\alpha > 0$ and $\beta > 0$ enforce the constraints $\mathbf{u} = \mathbf{f} - Q(\mathbf{f})$ and $\mathbf{v} = \nabla \mathbf{f}$. If $\alpha, \beta \rightarrow \infty$, we end up at the original problem (3). In order to strictly enforce the constraint, the Bregman variables \mathbf{b}_u and \mathbf{b}_v are

Algorithm 1 Denoising with the QuaSI prior using ADMM optimization

```

Initialize  $\mathbf{u}^1 = \mathbf{v}^1 = \mathbf{0}$ ,  $\mathbf{b}_u^1 = \mathbf{b}_v^1 = \mathbf{0}$  and  $\mathbf{f}_l^1 = \text{mean}(\mathbf{g}_l^{(1)}, \dots, \mathbf{g}_l^{(K)})$ 
for  $t = 1, \dots, T_{\text{outer}}$  do
    Assemble QuaSI linearization  $\mathbf{Q}$  from the intermediate estimate  $\mathbf{f}^t$  according to
    (7)
    for  $i = 1, \dots, T_{\text{inner}}$  do
        Update weight matrices  $\mathbf{W}^{(k)}$ ,  $k = 1, \dots, K$  for IRLS (14)
        Update the intermediate estimate  $\mathbf{f}^{t+1}$  using CG iterations for (11)
        Update the auxiliary variables  $\mathbf{u}^{t+1}$  and  $\mathbf{v}^{t+1}$  using (15) – (16)
        Update the Bregman variables  $\mathbf{b}_u^{t+1}$  and  $\mathbf{b}_v^{t+1}$  using (17) – (18)
    end for
end for

```

introduced. Then, we minimize the augmented Lagrangian:

$$\begin{aligned}
\mathcal{L}_{\text{AL}}(\mathbf{f}, \mathbf{u}, \mathbf{v}, \mathbf{b}_u, \mathbf{b}_v) = & \sum_{k=1}^K \rho(\mathbf{f} - \mathbf{g}^{(k)}) \\
& + \frac{\alpha}{2} \|\mathbf{u} - \mathbf{f} + Q(\mathbf{f}) - \mathbf{b}_u\|_2^2 + \lambda \|\mathbf{u}\|_1 \\
& + \frac{\beta}{2} \|\mathbf{v} - \nabla \mathbf{f} - \mathbf{b}_v\|_2^2 + \mu \|\mathbf{v}\|_1.
\end{aligned} \tag{10}$$

We iteratively optimize (10) by alternating minimization w.r.t. the individual parameters. Hence, three subproblems emerge, where the L_1 -Norm is decoupled from the L_2 -Norm. We solve these problems separately in alternating minimization scheme.

The minimization of the augmented Lagrangian (10) w.r.t. \mathbf{f} can be solved in a least square sense. Therefore, the binary matrix \mathbf{Q} is constructed using the result \mathbf{f}^t from the previous iteration, where t denotes the iteration index. In order to cope with the Huber loss, iteratively re-weighted least squares (IRLS) is applied. Solving the resulting least squares problem leads to the linear system:

$$\mathbf{A}\mathbf{f}^{t+1} = \mathbf{b} \tag{11}$$

$$\mathbf{A} = 2 \sum_{k=1}^K (\mathbf{W}^{(k)})^\top + \beta \nabla^\top \nabla + \alpha \mathbf{M}^\top \mathbf{M} \tag{12}$$

$$\mathbf{b} = 2 \sum_{k=1}^K (\mathbf{W}^{(k)})^\top \mathbf{g}^{(k)} + \beta \nabla^\top (\mathbf{v} - \mathbf{b}_v) + \alpha (\mathbf{M})^\top (\mathbf{u} - \mathbf{b}_u), \tag{13}$$

where $\mathbf{M} = \mathbf{I} - \mathbf{Q}$ and $\mathbf{W}^{(k)}$ are diagonal weight matrices constructed from \mathbf{f}^t . Using the intermediate result \mathbf{f}^t , we can computed the weights for IRLS according to:

$$W_{ii}^{(k)} = \frac{\phi'(f_i^t - g_i^{(k)})}{|f_i^t - g_i^{(k)}|}, \tag{14}$$

where $\phi'(z)$ is the derivative of the Huber loss. The threshold of the Huber loss is set $\epsilon = 1.345\sigma$ to achieve 95-percent efficiency of the estimator under Gaussian noise [18]. We use the mean absolute deviation (MAD) to estimate the standard deviation $\sigma = 1.4826\text{mad}(f_i^t - g_i^{(k)})$ [23]. To solve the linear system (11), conjugate gradient (CG) iterations are used.

The minimization of the augmented Lagrangian (10) w.r.t. the auxiliary variables can be done by exploiting the separability of the problem. Given the estimate for the intermediate result \mathbf{f}^{t+1} , this leads to the element-wise updates:

$$u_i^{t+1} = \text{shrink}([\mathbf{f}^{t+1} - \mathbf{Q}\mathbf{f}^{t+1} + \mathbf{b}_u^t]_i, \lambda/\alpha), \quad (15)$$

$$v_i^{t+1} = \text{shrink}([\nabla\mathbf{f}^{t+1} + \mathbf{b}_v^t]_i, \mu/\beta), \quad (16)$$

where $\text{shrink}(z, \gamma) = \text{sign}(z) \max(z - \gamma, 0)$ denotes the shrinkage operator [10].

Given an estimate for the intermediate result \mathbf{f}^{t+1} as well as the auxiliary variables \mathbf{u}^{t+1} and \mathbf{v}^{t+1} , the Bregman variables are updated according to:

$$\mathbf{b}_u^{t+1} = \mathbf{b}_u^t + (\mathbf{f}^{t+1} - \mathbf{Q}\mathbf{f}^{t+1} - \mathbf{u}^{t+1}), \quad (17)$$

$$\mathbf{b}_v^{t+1} = \mathbf{b}_v^t + (\nabla\mathbf{f}^{t+1} - \mathbf{v}^{t+1}). \quad (18)$$

Algorithm 1 summarizes the proposed ADMM based iteration scheme. Overall, we use two nested optimization loops to solve (8). We use the mean of the input images as an initial guess \mathbf{f}^1 as well as $\mathbf{u}^1 = \mathbf{v}^1 = \mathbf{0}$, $\mathbf{b}_u^1 = \mathbf{b}_v^1 = \mathbf{0}$. The weight matrices for IRLS are updated in every iteration step.

The linearization \mathbf{Q} of the quantile filter is updated every T_{inner} iterations, assuming the position of the quantile does not change within the next T_{inner} iterations. This assumption speeds up the algorithm, as the construction of the matrix is time-consuming. Note that T_{inner} should not be chosen too large in order to avoid a bad approximation of the quantile filter. A proper evaluation of the convergence of the algorithm is presented in Sect. 6.5.

6 Experiments and Results

In this section, we evaluate our spatio-temporal framework for denoising of retinal OCT data. Specifically, we quantitatively benchmark our method on different datasets including comparisons to the state-of-the-art. In addition to OCT, we also present an application of our QuaSI prior for removing structured noise in C-arm CT imaging.

Throughout all experiments, we adopted our framework in two versions. For denoising on a B-scan level, the parameters were set to $\mu = 0.075 \cdot K$, $\lambda = 5.0 \cdot K$, $\alpha = 100.0 \cdot K$, $\beta = 1.5 \cdot K$, $T_{\text{outer}} = 20$ and $T_{\text{inner}} = 2$ for K B-scans and 3×3 median filtering to setup the QuaSI prior. For volumetric denoising based on 6 adjacent B-scans, the parameters were set to $\mu = 0.0007 \cdot K$, $\lambda = 1.0 \cdot K$, $\alpha = 120.0 \cdot K$, $\beta = 0.05 \cdot K$, $T_{\text{outer}} = 20$ and $T_{\text{inner}} = 2$ for K volumes and $3 \times 3 \times 3$ median filtering.

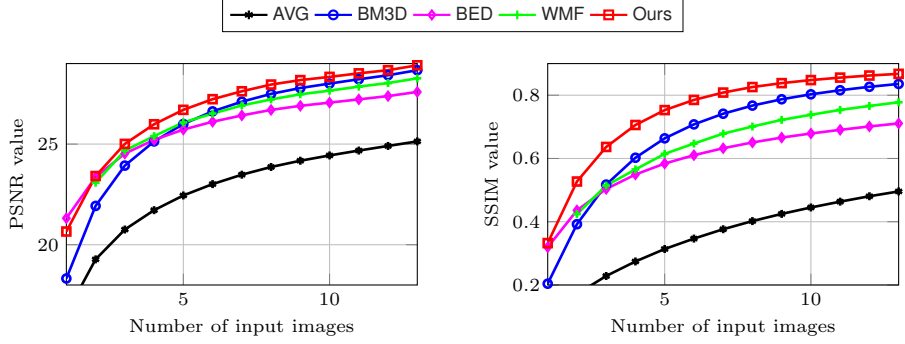


Fig. 5: Quantification of noise reduction in terms of mean PSNR and SSIM for different denoising methods on the pig eye dataset for different numbers of input images.

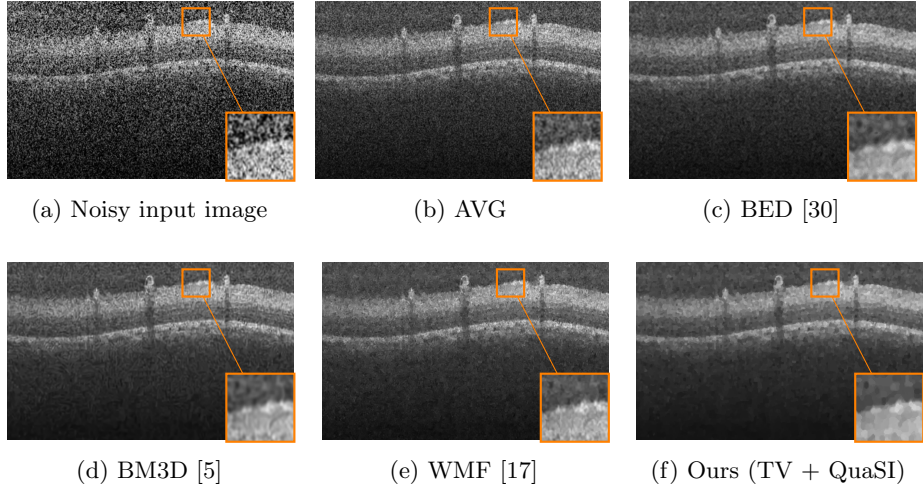


Fig. 6: Denoising on the pig eye dataset 9 using $K = 5$ B-scans. (a) Noisy image, (b) – (f) AVG, BED [30], BM3D [5], WMF [17], and the proposed method.

6.1 Datasets

To evaluate the performance of the proposed OCT denoising algorithm, we conducted experiments on two different datasets. This comprises ex-vivo benchmark data as well as real clinical data.

Pig Eye Data For an evaluation of OCT denoising on B-scan level, we used the publicly available pig eye dataset provided by Mayer *et al.* [17]. The dataset comprises 455 B-scans corresponding to 35 eye positions with 13 B-scans per

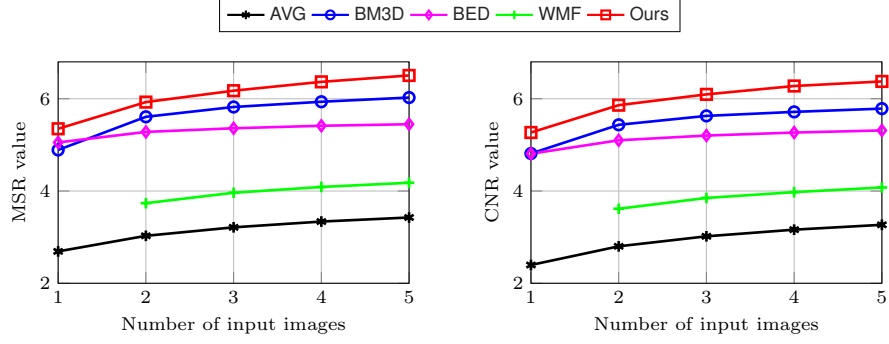


Fig. 7: Quantification of noise reduction in terms of mean MSR and CNR measures for denoising on a B-scan level on our clinical dataset for different numbers of input images.

position and was captured ex-vivo with a Spectralis HRA & OCT. The published B-scans were registered to each other to compensate for geometric shifts between them. We apply denoising to sets of K registered B-scans with $K \in [1, 13]$ to demonstrate the influence of different numbers of input B-scans on the denoising result.

The pig eye dataset provides a gold standard B-scans that was obtained by averaging all 455 registered scans. The quality of the denoising algorithm was evaluated by assessing the fidelity of a denoised B-scan w.r.t. to the gold standard using the peak-signal-to-noise ratio (PSNR) as well as the structural similarity index (SSIM).

Clinical Data In order to evaluate and compare B-scan with volumetric denoising, we use clinical data. A prototype ultrahigh-speed swept-source OCT system with 1050 nm wavelength and a sampling rate of 400,000 A-scans per second [29] was used to acquire volumetric data of 14 human subjects. Proliferative and non-proliferative diabetic retinopathy, early age-related macular degeneration and one healthy subject are covered on two volumes per subject, where each B-scan was acquired five times in immediate succession. We use 500 A-scans by 500 B-scans for a field size of 3×3 mm.

For denoising on a B-scan level the central B-scan of each volume is used, while volumetric denoising is performed on adjacent B-scans including the central one. As the clinical data does not provide a gold standard, we follow prior work [9,19,30] and the measure noise reduction using the mean-to-standard-deviation

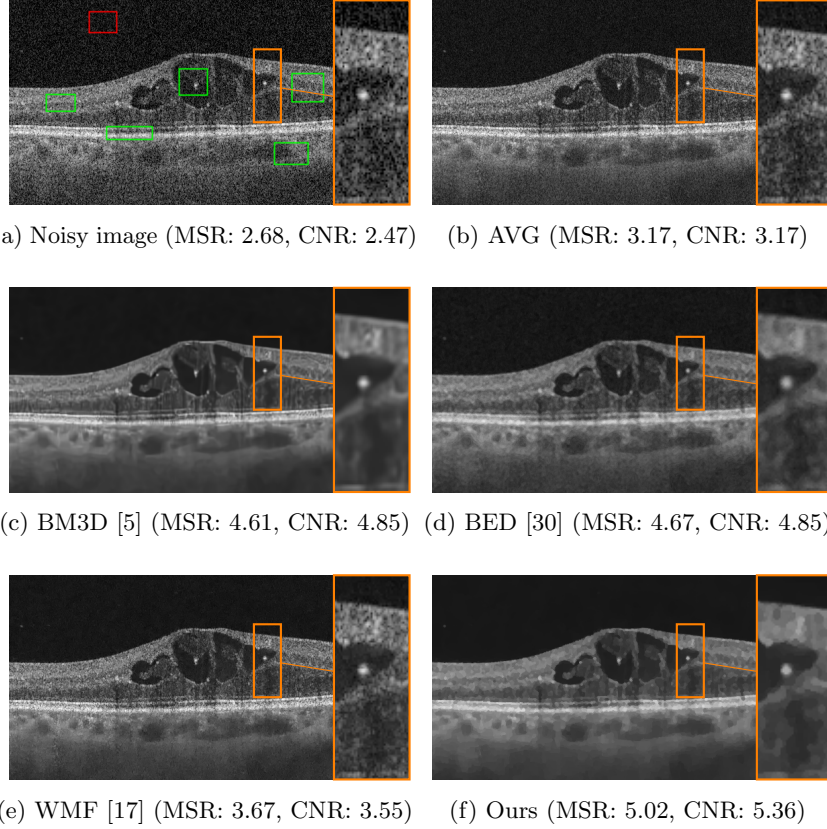


Fig. 8: Visual comparison of denoising results using our clinical dataset with $K = 5$ B-scans from a 46 years old male diabetic retinopathy patient. (a) Noisy image with manually selected background (red) and foreground (green) to determine MSR and CNR. (b) – (f) AVG, BM3D [5], BED [30], WMF [17], and the proposed method.

ratio (MSR) and the contrast-to-noise ratio (CNR) according to:

$$\text{MSR} = \frac{\mu_f}{\sigma_f} \quad (19)$$

$$\text{CNR} = \frac{|\mu_f - \mu_b|}{\sqrt{\frac{1}{2}(\sigma_f^2 + \sigma_b^2)}}, \quad (20)$$

where μ_f and μ_b as well as σ_f and σ_b denote the means and standard deviations of the intensities in a foreground and a background region, respectively. The regions to determine MSR and CNR were manually selected for the central B-scan of each volume, see Fig. 8a.

6.2 Comparison to the State-of-the-art

We compared our proposed spatio-temporal denoising against four competing noise reduction approaches. As a representative of general-purpose methods, we evaluated the popular BM3D [5] that is state-of-the-art in the field of natural image denoising. In terms of spatial filters customized for OCT, we used Bayesian estimation denoising (BED) [30]. In the field of temporal methods using multiple registered B-scans, we evaluate simple averaging (AVG) as a baseline as well as wavelet multi-frame denoising (WMF) [17]. To ensure fair comparisons between spatial and temporal methods, we provide the average of all B-scans as input for single-image denoising (BM3D and BED). In contrast, AVG and WMF are pure temporal approaches that process multiple registered B-scans. Notice that all of these methods can only operate on individual 2-D B-scans to denoise volumetric data and are therefore compared to our proposed method on a B-scan level.

First, we conducted experiments for denoising on a B-scan level on the pig eye dataset described in Section 6.1. Figure 5 depicts the mean PSRN and SSIM of the competing denoising methods w.r.t. to the gold standard for different numbers of input B-scans. We observed quantitatively that our proposed method consistently outperforms the competing BM3D, BED, and WMF denoising regardless of the number of input frames. Moreover, using only 2 input B-scans, our spatio-temporal method achieved comparable results to averaging 5 B-scans. This reveals that our method is more economic regarding the number of required input scans. This property is essential for clinical applications, where acquiring more scans might lead to unacceptable long acquisition times. Figure 6 depicts qualitative denoising results for $K = 5$ B-scans. Here, the proposed spatio-temporal denoising algorithm using the QuaSI prior achieved superior performance in terms of noise reduction, while anatomical structures like retinal layers are preserved. Second, denoising on a B-scan level was studied on our clinical datasets using the non-reference MSR and CNR measures for a quantitative evaluation. Figure 7 depicts the averaged MSR and CNR measures for different numbers of input images. Overall, we observed that BM3D and our proposed method achieved the best noise reduction expressed by both measures. Figure 8 qualitatively compares the denoising performance on one example dataset. We found that AVG, WMF, BED facilitate structure-preserving denoising but were prone to noise breakthroughs in homogeneous areas, which lowers their MSR and CNR. In contrast, BM3D achieved superior noise reduction but suffered from streak artifacts. Similar observations were made in related work on OCT denoising [9] and can be explained by assumption of additive white Gaussian noise used for BM3D. The proposed method achieved a decent tradeoff between noise reduction and structure preservation.

6.3 Impact of the QuaSI Prior

We used the pig eye dataset as well as the clinical data to evaluate the performance of our spatio-temporal denoising algorithm with and without the QuaSI prior. Fig. 9 illustrates the impact of the QuaSI prior on the denoising result for the

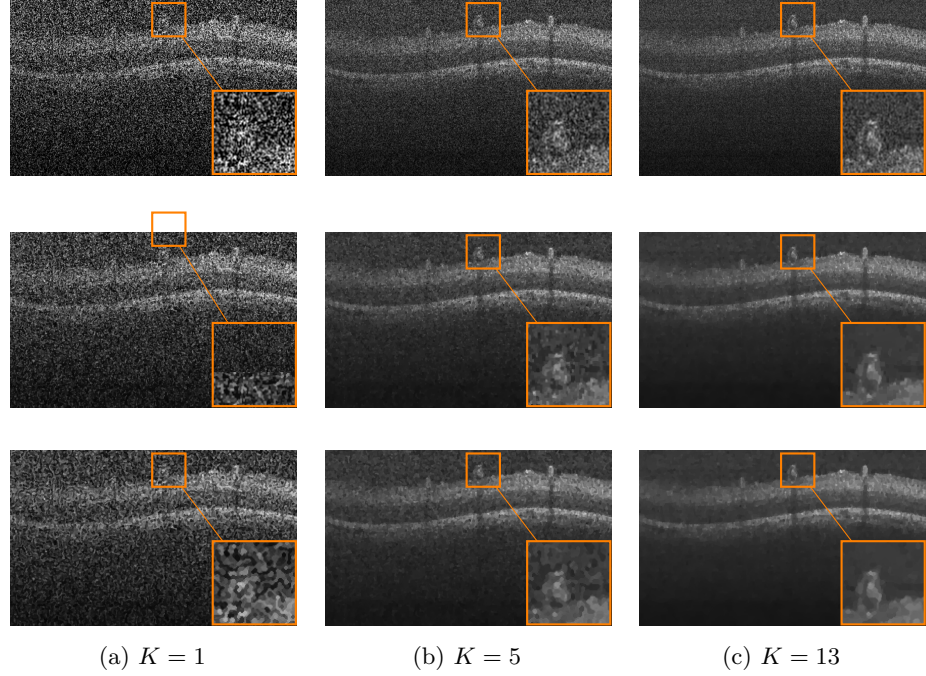


Fig. 9: This comparison aims at demonstrating the improvement of the proposed spatio-temporal denoising with TV + QuaSI regularization (third row) compared to simple averaging of consecutive B-scans (top row) and the proposed spatio-temporal denoising with TV regularization only (second row) for different numbers of input images.

Fig. 9 illustrates the impact of the QuaSI prior using PSNR and SSIM (for the pig eye data) as well as MSR and CNR (for clinical data) for different numbers of input scans. Here, our denoising framework with QuaSI prior outperformed TV denoising in terms of all measures.

Fig. 10 illustrates the impact of the QuaSI prior using PSNR and SSIM (for the pig eye data) as well as MSR and CNR (for clinical data) for different numbers of input scans. Here, our denoising framework with QuaSI prior outperformed TV denoising in terms of all measures.

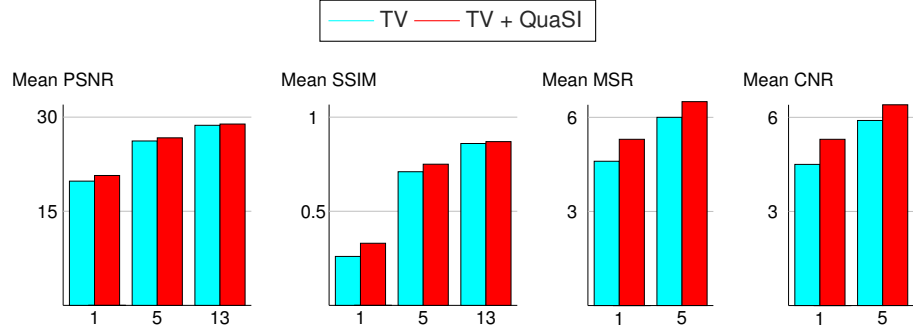


Fig. 10: Mean PSNR, SSIM, MSR and CNR measures to quantify noise reduction with and without the QuaSI prior for 1, 5 and 13 input images.

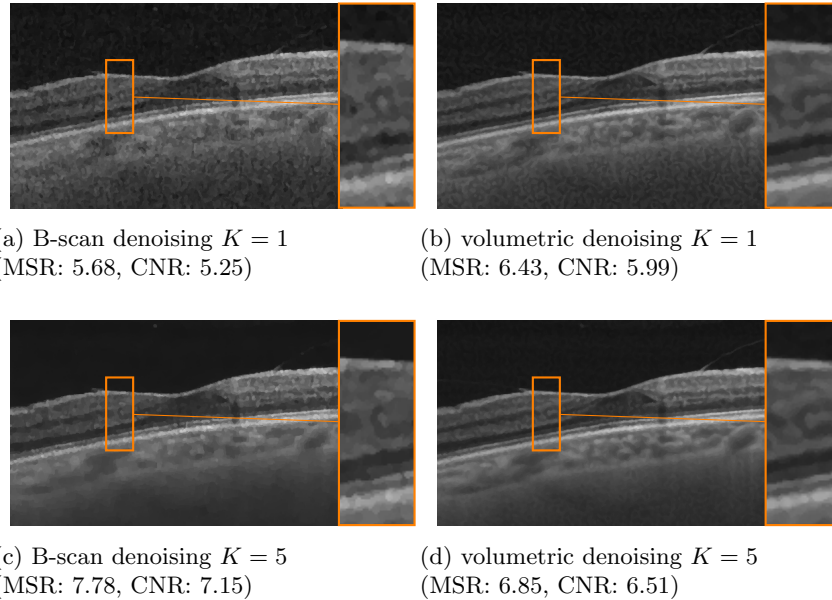


Fig. 11: Denoising on the clinical dataset using 5 registered volumes from a 67 years old male mild non-proliferative diabetic retinopathy patient. Denoising is performed on a B-scan level as well as on a volume level.

6.4 B-scan vs. Volumetric Denoising

So far, we evaluated denoising of volumetric OCT data by simply processing individual B-scans. In order to evaluate the impact of true volumetric denoising to simple B-scan wise B-scan denoising in our proposed framework, we used the clinical dataset presented in Section 6.1. Our volumetric denoising processes 6

	$K = 1$ scan		$K = 5$ scans	
	B-scan denoising	Volumetric denoising	B-scan denoising	Volumetric denoising
MSR	5.35	5.77	6.50	6.31
CNR	5.27	5.60	6.38	6.18

Table 1: Mean MSR and CNR measures for 1 and 5 registered input volumes on the clinical data. For B-scan denoising, the central B-scan is used and for volumetric denoising 6 adjacent B-scans including the central one are used.

consecutive B-scans including the central one. That way, CNR and MSR measures from the previous experiments can be used for comparison. Table 1 shows the mean MSR and CNR using one and five registered input volumes. Here, we found that our volumetric denoising achieved better results in terms of noise reduction for 1 input volume, as adjacent B-scans affect denoising positively. For 5 input volumes, we found that our B-scan denoising achieved slightly better results in terms of noise reduction. However, as opposed to noise reduction, volumetric denoising achieved superior performance in structure preservation by exploiting coherence between adjacent B-scans. This is depicted in Fig. 11, where the retinal layers in the magnified region can be better distinguished.

6.5 Convergence and Parameter Sensitivity

The convergence of the proposed algorithm is shown experimentally on a B-scan level. By our definition, the algorithm converges if a stationary point of the objective function (3) is reached. The value of the objective, hereinafter referred to as energy, is computed after every update of the intermediate image \mathbf{f}^{t+1} . In addition, PSNR and SSIM of the intermediate image are computed. Based on the optimal parameter setting $\mu = 0.075 \cdot K$, $\lambda = 5.0 \cdot K$, $\alpha = 100.0 \cdot K$, $\beta = 1.5 \cdot K$, $T_{\text{outer}} = 20$, $T_{\text{inner}} = 10$ and $T_{\text{cg}} = 3$ for B-scan denoising, we denoise the pig eye dataset 9 with $K = 8$ B-scans. Varying one parameter in an otherwise fixed parameter setting shows the influence of the individual parameter on the convergence.

Fig. 12 illustrates the influence of T_{outer} , T_{inner} and T_{cg} on the convergence, where $T_{\text{outer}} \cdot T_{\text{inner}} = 300$ for fair comparison. Three different settings are compared, the optimal parameter setting, a special case where $T_{\text{inner}} = 1$ and large T_{cg} . The approximation of the QuaSI prior is updated every T_{inner} iterations. With increasing number of inner iterations, peaks appear in the energy as well as in the PSNR value and impair the convergence properties of the algorithm. This is mainly attributable to the rare assembly of \mathbf{Q} . Hence, the special case shows nice convergence properties, as no approximation is necessary. Due to the high computational costs of the special case, the proposed optimal setting is preferable. It requires half the computational cost with similar convergence properties. Furthermore, the PSNR value increases faster. Increasing T_{cg} also

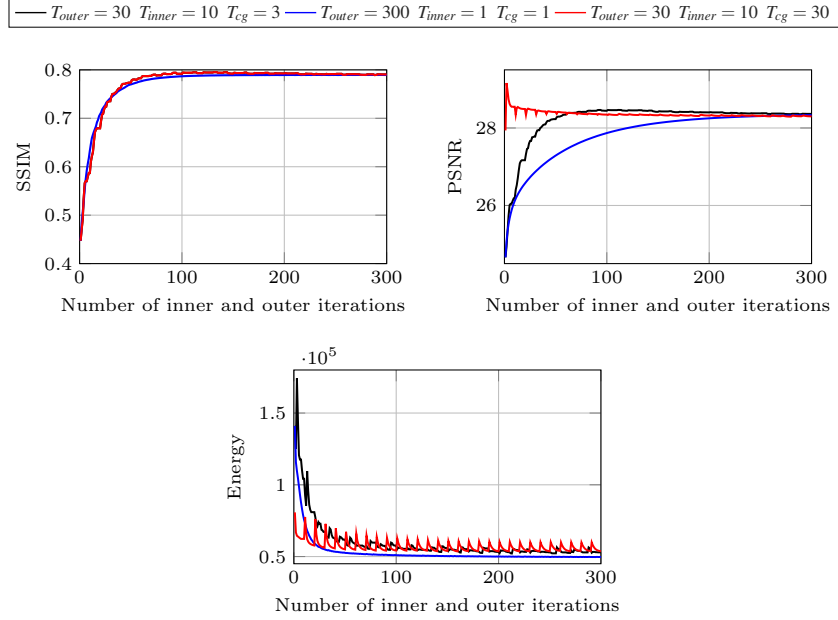


Fig. 12: The division of number of iterations on T_{outer} , T_{inner} and T_{cg} influences the convergence behavior of the proposed algorithm. The intermediate energy and PSNR measures of four different settings are displayed.

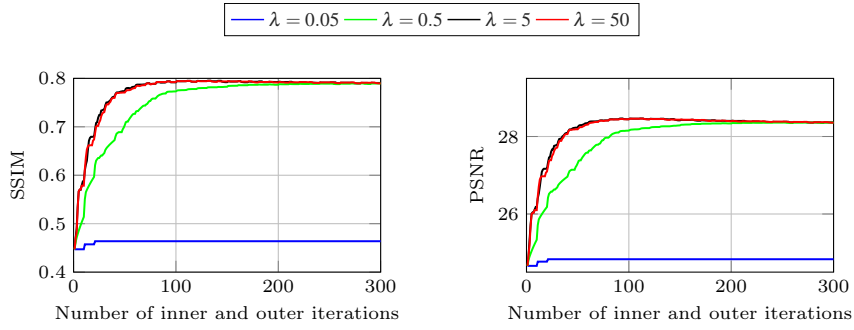


Fig. 13: Intermediate SSIM and PSNR measures of four different λ values to illustrate the impact of the QuaSI prior on the convergence behavior of the algorithm.

induces peaks in the energy and PSNR value. Additionally, the PSNR value decreases, which is not preferable.

The impact of the QuaSI prior on the denoising process is controlled by λ , which is illustrated in Fig. 13. With decreasing λ the PSNR and SSIM value increase slower, due to the low impact of the QuaSI prior. This underlines the

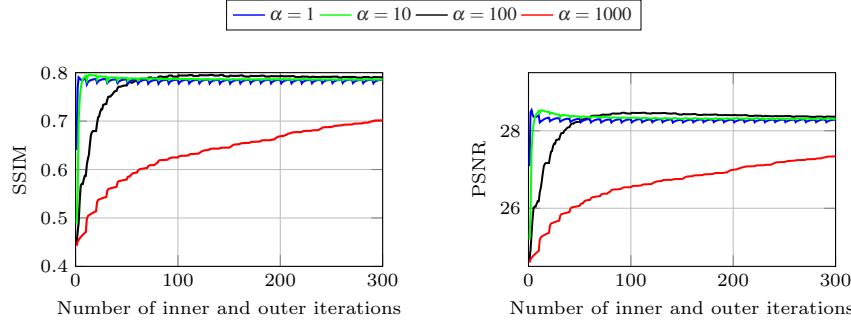


Fig. 14: Comparison of four different values for the Lagrangian multiplier α and their influence on the convergence behavior of the proposed algorithm. The intermediate energy and PSNR measures are displayed.

effectiveness of the proposed QuaSI prior. Increasing λ does not change the convergence properties of the algorithm.

The Lagrangian multiplier α enforces the constraint $\mathbf{u} = \mathbf{f} - \mathbf{Q}(\mathbf{f})$. For $\alpha \rightarrow \infty$, the augmented Lagrangian (10) results in the objective function (3). Hence, decreasing α impairs the convergence properties of the algorithm by introducing peaks in the SSIM as well as in the PSNR value. PSNR and SSIM value decrease, which is not preferable. Choosing a large $\alpha = 1000$ reduces the peaks but the PSNR value increases slower compared to the proposed parameter setting. For a large α , the constraint must be satisfied more strictly which results in higher computational cost due to the slow convergence.

6.6 Quantile Sparse Image Denoising for Volumetric C-Arm Data

Besides the OCT data presented in previous sections, we further applied the QuaSI framework for denoising cerebral perfusion data acquired using a C-arm computed tomography (CT) system. This data describes a sequence of volumetric CT images and is commonly used for stroke assessment by measuring the distribution of injected contrast agent within the brain over time. Photon effects as well as patient movement and angular undersampling usually deteriorates the image quality by introducing both structured and unstructured noise (see Figure 15 a,c).

Current approaches towards noise reduction in CT imaging are, for example, based on anisotropic filtering or rely on a heuristic detection of streaks and vessel structures [14,15,16].

Compared to OCT, where the proposed method takes multiple input images and results in a single output image, denoising of C-arm perfusion data transforms multiple input images to multiple output images, hereinafter called QuaSI 3-D+t. The constraint optimization problem, as given in (8), thus slightly changes by enforcing the data fidelity for each input volume and by incorporating an L_1 -Norm regularizer in temporal direction for subsequent volumes, resulting in

$$\hat{\mathbf{f}} = \underset{\mathbf{f}}{\operatorname{argmin}} \rho(\mathbf{f} - \mathbf{g}) + \lambda \|\mathbf{u}\|_1 + \mu \|\mathbf{v}\|_1 + \omega \|\mathbf{d}_t\|_1, \quad (21)$$

where \mathbf{f} and $\mathbf{g} \in \mathbb{R}^N$ with $N = N_x N_y N_z N_t$ describe a sequence of volumetric image data. In the last term of equation 21, $\omega \geq 0$ describes a weighting factor and $\mathbf{d}_t = \nabla_t \mathbf{f}$ the gradient in temporal direction, respectively. According to (9), the constraint optimization problem can thus be formulated as

$$\begin{aligned} \hat{\mathbf{f}} = \underset{\mathbf{f}}{\operatorname{argmin}} \rho(\mathbf{f} - \mathbf{g}) + & \frac{\alpha}{2} \|\mathbf{u} - \mathbf{f} + Q(\mathbf{f})\|_2^2 + \lambda \|\mathbf{u}\|_1 + \\ & \frac{\beta}{2} \|\mathbf{v} - \nabla \mathbf{f}\|_2^2 + \mu \|\mathbf{v}\|_1 + \frac{\gamma}{2} \|\mathbf{d}_t - \nabla_t \mathbf{f}\|_2^2 + \omega \|\mathbf{d}_t\|_1, \end{aligned} \quad (22)$$

and is solved using the optimization approach given in Section 5.

We applied the QuaSI denoising both on simulated C-arm CT data and on acquired, real patient data. The simulated data has been created using a digital brain CT phantom [1] and a realistic scanning protocol (133 projections over an angular range of 200° per volume). We added Poisson noise and introduced minor patient movement during the generation of the simulated data by moving the head up to 5° around z-axis between the individual scans. After reconstruction, the individual scans are co-registered again to assert pixel correspondence between the volumes.

	Input	BM4D	QuaSI	3-D+t
PSNR	32.105	32.485	34.788	
SSIM	0.883	0.914	0.943	

Table 2: PSNR and SSIM for the input data, BM4D [13] and the QuaSI method.

We compared the results from the proposed method to the results from BM4D [13], which is an extension of BM3D [6] to volumetric data. For a numerical comparison of the algorithms we calculate the peak signal to noise ratio (PSNR) and the structured similarity index measure (SSIM) [28]. We set the parameters of our method to $\alpha = 0.1$, $\lambda = 0.0006$, $\beta = 0.09$, $\mu = 0.004$, $\gamma = 90$ and $\omega = 0.8$. The median filter regularization is computed on a $3 \times 3 \times 3$ kernel.

The algorithms are applied to and evaluated on a subset of the brain volume consisting of 30 consecutive slices. The slices show the complete head and contain all structures of interest such as bones, white matter, gray matter and (contrast-enhanced) vessels. The results from the evaluation of the realistic brain phantom show that the proposed denoising algorithm outperforms BM4D with regards to

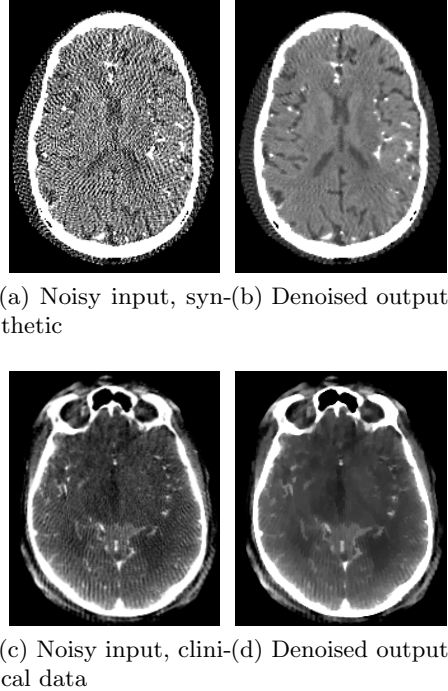


Fig. 15: Input to and result from the QuaSI method. (a) and (c) denote noisy input to the algorithm, (b) and (d) denote the denoised result. The upper and lower row shows synthetic and real data, respectively. Note that the input to the algorithm is not just the slice as shown in the figure, but consists of a sequence of volumetric data.

PSNR and SSIM, see Table 2. Vessel structures are well-preserved within both volumes and boundaries between gray and white matter are perceivable.

Fig. 15 shows the input data and results from the QuaSI method for a single slice out of one of the volume sequence.

7 Conclusion

In this paper, we have presented the quantile sparse image (QuaSI) prior and a corresponding spatio-temporal denoising algorithm suitable for volumetric OCT or CT data. For OCT denoising, we proposed two pipelines to either process B-scans or volumetric OCT data. The numerical optimization is derived using a linearization of the quantile filter and an alternating direction method of multipliers scheme for efficient minimization. We can show that a combination of QuaSI and Total Variation regularization outperforms state-of-the-art methods in terms of quantitative measures. Interestingly, our method can be applied to

both CT and OCT data through minor modifications of the denoising pipeline. This suggests that it may be worthwhile to evaluate the potential of the QuaSI prior for inverse problems of other imaging modalities in future work.

References

References

1. Aichert, A., Manhart, M.T., Navalpakkam, B.K., Grimm, R., Hutter, J., Maier, A.K., Hornegger, J., Doerfler, A.: A realistic digital phantom for perfusion c-arm CT based on MRI data. In: Nuclear Science Symposium and Medical Imaging Conference (NSS/MIC), 2013 IEEE. pp. 1–2. IEEE (2013)
2. Bian, L., Suo, J., Chen, F., Dai, Q.: Multiframe denoising of high-speed optical coherence tomography data using interframe and intraframe priors. *Journal of Biomedical Optics* 20, 20 – 20 – 11 (2015)
3. Burger, H.C., Schuler, C.J., Harmeling, S.: Image denoising: Can plain neural networks compete with bm3d? In: IEEE Conference on Computer Vision and Pattern Recognition. pp. 2392–2399 (June 2012)
4. Cheng, J., Duan, L., Wong, D.W.K., Tao, D., Akiba, M., Liu, J.: Speckle Reduction in Optical Coherence Tomography by Image Registration and Matrix Completion. In: MICCAI 2014, Proceedings, Part I. pp. 162–169 (2014)
5. Dabov, K., Foi, A., Katkovnik, V., Egiazarian, K.: Image denoising by sparse 3-d transform-domain collaborative filtering. *IEEE Trans. Image Process.* 16(8), 2080–2095 (2007)
6. Dabov, K., Foi, A., Katkovnik, V., Egiazarian, K.: Image denoising by sparse 3-d transform-domain collaborative filtering. *IEEE Trans. Image Process.* 16(8), 2080–2095 (2007)
7. Desjardins, A.E., Vakoc, B.J., Oh, W.Y., Motaghiannezam, S.M., Tearney, G.J., Bouma, B.E.: Angle-resolved optical coherence tomography with sequential angular selectivity for speckle reduction. *Opt. Express* 15(10), 6200 (2007)
8. Duan, J., Lu, W., Tench, C., Gottlob, I., Proudlock, F., Samani, N.N., Bai, L.: Denoising optical coherence tomography using second order total generalized variation decomposition. *Biomed. Signal Process Control* 24, 120–127 (2016)
9. Fang, L., Li, S., Nie, Q., Izatt, J.A., Toth, C.A., Farsiu, S.: Sparsity based denoising of spectral domain optical coherence tomography images. *Biomed. Opt. Express* 3(5), 927–942 (2012)
10. Goldstein, T., Osher, S.: The split bregman method for l1-regularized problems. *SIAM J. Imaging Sci.* 2(2), 323–343 (2009)
11. Köhler, T., Huang, X., Schebesch, F., Aichert, A., Maier, A., Hornegger, J.: Robust Multiframe Super-Resolution Employing Iteratively Re-Weighted Minimization. *IEEE Transactions on Computational Imaging* 2(1), 42 – 58 (Mar 2016)
12. Kraus, M.: Motion Correction and Signal Enhancement in Optical Coherence Tomography. Ph.D. thesis, Friedrich-Alexander-Universität Erlangen-Nürnberg (FAU) (2016)
13. Maggioni, M., Katkovnik, V., Egiazarian, K., Foi, A.: Nonlocal transform-domain filter for volumetric data denoising and reconstruction. *IEEE Trans. Image Process.* 22(1), 119–133 (2013)

14. Maier, A., Fahrig, R.: GPU Denoising for Computed Tomography, vol. 1. CRC Press, Boca Raton, Florida, USA, 1 edn. (2015), <http://www.crcnetbase.com/doi/10.1201/b18968-9>
15. Maier, A., Wigström, L., Hofmann, H., Hornegger, J., Zhu, L., Strobel, N., Fahrig, R.: Three-dimensional anisotropic adaptive filtering of projection data for noise reduction in cone beam CT. *Medical Physics* 38(11), 5896–5909 (2011), <http://www5.informatik.uni-erlangen.de/Forschung/Publikationen/2011/Maier11-TAA.pdf>
16. Manhart, M., Fahrig, R., Hornegger, J., Dörfler, A., Maier, A.: Guided Noise Reduction for Spectral CT with Energy-Selective Photon Counting Detectors. In: Noo, F. (ed.) *Proceedings of the Third CT Meeting*. pp. 91–94 (2014), <https://www5.informatik.uni-erlangen.de/Forschung/Publikationen/2014/Manhart14-GNR.pdf>
17. Mayer, M.A., Borsdorf, A., Wagner, M., Mardin, C.Y., Tornow, R.P.: Wavelet denoising of multiframe optical coherence tomography. *Biomed Opt Express* 3(3), 2156–7085 (2012)
18. Ochs, P., Dosovitskiy, A., Brox, T., Pock, T.: On iteratively reweighted algorithms for nonsmooth nonconvex optimization in computer vision. *SIAM J. Imaging Sci.* 8(1), 331–372 (2015)
19. Ozcan, A., Bilenca, A., Desjardins, A.E., Bouma, B.E., Tearney, G.J.: Speckle reduction in optical coherence tomography images using digital filtering. *Journal of the Optical Society of America A* 24(7), 1901 (2007)
20. Pan, J., Sun, D., Pfister, H., Yang, M.H.: Blind image deblurring using dark channel prior. In: *CVPR, Proceedings*. pp. 1628–1636 (2016)
21. Pircher, M., Gotzinger, E., Leitgeb, R., Fercher, A.F., Hitzenberger, C.K.: Speckle reduction in optical coherence tomography by frequency compounding. *J. Biomed. Opt.* 8(3), 565 (2003)
22. Romano, Y., Elad, M., Milanfar, P.: The Little Engine that Could: Regularization by Denoising (RED). *arXiv preprint arXiv:1611.02862* (2016)
23. Rousseeuw, P.J., Leroy, A.M.: *Robust Regression and Outlier Detection*. John Wiley & Sons (1987)
24. Salinas, H.M., Fernandez, D.C.: Comparison of PDE-Based Nonlinear Diffusion Approaches for Image Enhancement and Denoising in Optical Coherence Tomography. *IEEE Trans. Med. Imag.* 26(6), 761–771 (2007)
25. Schirrmacher, F., Köhler, T., Husvogt, L., Fujimoto, J.G., Hornegger, J., Maier, A.K.: Quasi: Quantile sparse image prior for spatio-temporal denoising of retinal OCT data. In: *MICCAI 2017, Proceedings, Part II*. pp. 83–91 (2017)
26. Thapa, D., Raahemifar, K., Lakshminarayanan, V.: Reduction of speckle noise from optical coherence tomography images using multi-frame weighted nuclear norm minimization method. *Journal of Modern Optics* 62(21), 1856–1864 (2015)
27. Tomasi, C., Manduchi, R.: Bilateral Filtering for Gray and Color Images. In: *International Conference on Computer Vision (ICCV)*. pp. 839–846. IEEE, Bombay, India (Jan 1998)
28. Wang, Z., Bovik, A.C., Sheikh, H.R., Simoncelli, E.P.: Image quality assessment: from error visibility to structural similarity. *IEEE Trans. Image Process.* 13(4), 600–612 (2004)
29. W.Chi, Potsaid, B., Jayaraman, V., Baumann, B., Grulkowski, I., Liu, J.J., Lu, C.D., Cable, A.E., Huang, D., Duker, J.S., Fujimoto, J.G.: Phase-sensitive swept-source optical coherence tomography imaging of the human retina with a vertical cavity surface-emitting laser light source. *Opt Lett* 38(3), 338 (2013)

30. Wong, A., Mishra, A., Bizheva, K., Clausi, D.A.: General bayesian estimation for speckle noise reduction in optical coherence tomography retinal imagery. *Opt. Express* 18(8), 8338–8352 (2010)